TOPOLOGICAL MATTER

Magnetic Weyl semimetal phase in a Kagomé crystal

D. F. Liu[1,2]*, A. J. Liang[2,3,4]*, E. K. Liu[5,6]*, Q. N. Xu[5]*, Y. W. Li[7], C. Chen[2,3,7], D. Pei[7], W. J. Shi[2], S. K. Mo[4], P. Dudin[8], T. Kim[8], C. Cacho[8], G. Li[2,3], Y. Sun[5], L. X. Yang[9], Z. K. Liu[2,3], S. S. P. Parkin[1], C. Felser[5,10,11], Y. L. Chen[2,3,7,9]†

Weyl semimetals are crystalline solids that host emergent relativistic Weyl fermions and have characteristic surface Fermi-arcs in their electronic structure. Weyl semimetals with broken time reversal symmetry are difficult to identify unambiguously. In this work, using angle-resolved photoemission spectroscopy, we visualized the electronic structure of the ferromagnetic crystal $Co_3Sn_2S_2$ and discovered its characteristic surface Fermi-arcs and linear bulk band dispersions across the Weyl points. These results establish $Co_3Sn_2S_2$ as a magnetic Weyl semimetal that may serve as a platform for realizing phenomena such as chiral magnetic effects, unusually large anomalous Hall effect and quantum anomalous Hall effect.

The past decade has witnessed exciting progress in condensed-matter physics: relativistic phenomena can be simulated in easily available tabletop materials (*1*–*5*), and the principles of topology can be used for the discovery of materials with exotic physical properties (*3*–*5*).

One such class of materials are Weyl semimetals (WSMs), which host emergent Weyl fermions in the bulk and surface Fermi arc (SFA) states that connect the Weyl points of opposite chirality (*6*–*11*). This can give rise to unusual physical phenomena (*12*–*16*) and even inspire theoretical progress (*17*–*20*). In solids, WSMs can exist in crystals that break the time-reversal symmetry (TRS) (*5*, *6*, *21*, *22*), the inversion symmetry (IS) (*7*–*11*, *23*), or both (*24*). Compared with the IS-breaking WSMs (*9*–*11*, *25*–*28*), TRS-breaking WSMs provide a playground for the interplay among magnetism, electron correlation, and topological orders, which can give rise to rich exotic quantum states (Fig. 1A) ranging from quantum anomalous Hall (QAH) effects to axion insulators (*5*, *6*, *29*–*31*).

TRS-breaking WSMs have other preferred properties. For example, chiral anomaly is easier to observe in materials that have only two Weyl points (*5*, *32*), which is possible only in TRS-breaking WSMs [Fig. 1B (i)]; by contrast, time-reversal invariant IS-breaking WSMs have a minimum of four Weyl points [Fig. 1B (ii)] (*5*). Additionally, by preserving the IS, the energies of a pair of Weyl points in a TRS-breaking WSM are required to be the same (*5*), making it possible to realize the true nodal WSM phase when the Fermi energy coincides with the Weyl nodes. Finally, the TRS-breaking WSMs are attractive for spintronics applications, as the enhanced Berry curvature, together with its intrinsic magnetism, may lead to unusually large anomalous Hall conductivity (AHC) and anomalous Hall angle (AHA) (*33*, *34*).

However, despite the many proposed candidates (*6*, *21*, *22*, *35*–*38*), unambiguous and direct experimental confirmation of TRS-breaking WSMs remains challenging.

Recently, a ferromagnetic Shandite $Co_3Sn_2S_2$ was proposed to be a TRS-breaking WSM with three pairs of Weyl points in its three-dimensional (3D) Brillouin zone (BZ) (*33*, *39*). The transport

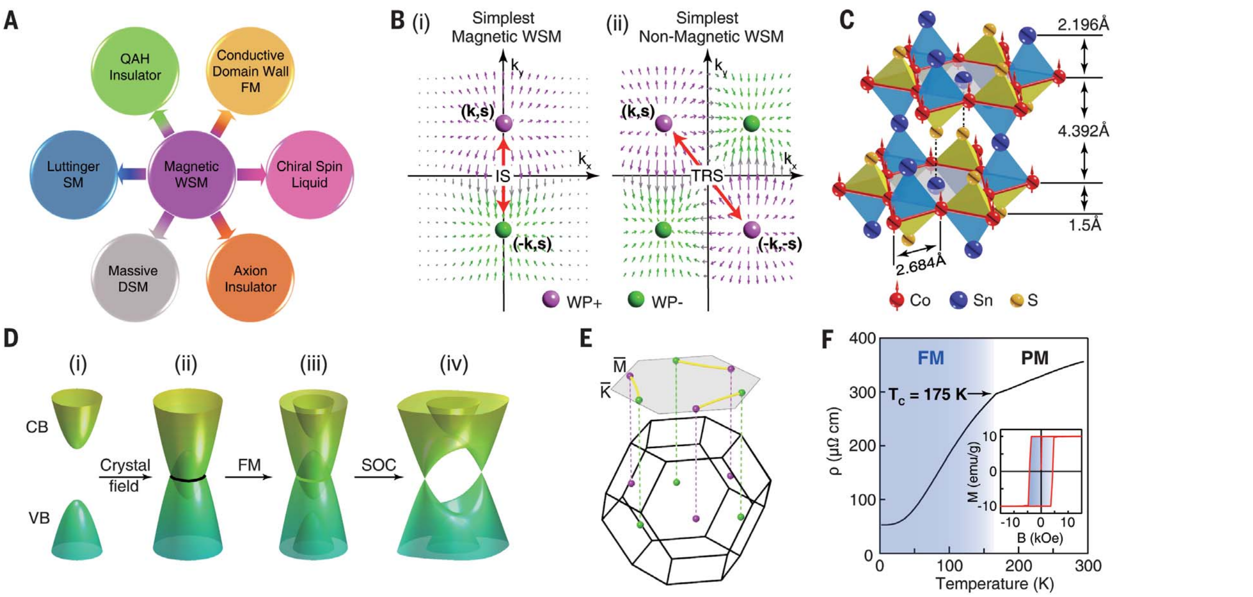

Fig. 1. $Co_3Sn_2S_2$ as a candidate magnetic WSM. (**A**) Exotic neighboring states of the magnetic WSM can be achieved by tuning parameters such as magnetism, thickness, and electron correlation (see text for more details). SM, semimetal; DSM, Dirac semimetal; WSM, Weyl semimetal; QAH, quantum anomalous Hall; FM: ferromagnetism. (**B**) Comparison between (i) simplest magnetic WSMs (with one pair or two Weyl points) and (ii) simplest nonmagnetic WSMs (with two pairs or four Weyl points). Magenta and green color of the Weyl points represent positive (+) and negative (−) chirality, respectively; the arrows illustrate the Berry curvature. ***k***, momentum; ***s***, spin; WP, Weyl point; IS, inversion symmetry; TRS, time reversal symmetry. (**C**) Crystal structure of $Co_3Sn_2S_2$, showing the stacked …–Sn-[S-(Co_3-Sn)-S]–… layers. (**D**) Mechanism for the magnetic WSM phase in $Co_3Sn_2S_2$ (see text for details). CB, conduction band; VB, valence band; FM, ferromagnetism; SOC, spin-orbital coupling. (**E**) Schematic of the bulk and surface Brillouin zones along the (001) surface of $Co_3Sn_2S_2$, with the Weyl points marked and connected by SFAs (yellow line segments). (**F**) Temperature dependences of longitudinal electric resistivity. The ferromagnetic transition occurs at T_C = 175 K, as indicated by the kink in the curve. Inset: Hysteresis loop of the magnetization (external magnetic field is along the *z* axis) measured at *T* = 2 K, showing a typical ferromagnetic behavior. PM, paramagnetism.

measurements have demonstrated an unusually large AHC and large AHA (*33*, *34*) in this material, making it a promising magnetic WSM candidate. The electronic band structure obtained from theory has shown similarity to previous experiments (*34*); however, direct evidence for WSMs, such as the existence of bulk Weyl points with linear dispersions, and the SFAs, is still missing. Here, we used angle-resolved photoemission spectroscopy (ARPES) to systematically study the electronic structures of single-crystal $Co_3Sn_2S_2$ and observed the characteristic SFAs and the bulk Weyl points in the ferromagnetic phase. These findings, further supported by excellent agreement with ab initio calculations, confirm the TRS-breaking WSM phase in $Co_3Sn_2S_2$ and provide important insights for the understanding of its exotic physical properties [see discussion in (*40*) for details].

[1]Max Planck Institute of Microstructure Physics, Halle 06120, Germany. [2]School of Physical Science and Technology, Shanghai Tech University, Shanghai 201210, China. [3]ShanghaiTech Laboratory for Topological Physics, Shanghai 200031, China. [4]Advanced Light Source, Lawrence Berkeley National Laboratory, Berkeley, CA 94720, USA. [5]Max Planck Institute for Chemical Physics of Solids, Dresden D-01187, Germany. [6]Institute of Physics, Chinese Academy of Sciences, Beijing 100190, China. [7]Clarendon Laboratory, Department of Physics, University of Oxford, Oxford OX1 3PU, UK. [8]Diamond Light Source, Didcot OX11 0DE, UK. [9]State Key Laboratory of Low Dimensional Quantum Physics, Department of Physics and Collaborative Innovation Center of Quantum Matter, Tsinghua University, Beijing 100084, China. [10]John A. Paulson School of Engineering and Applied Sciences, Harvard University, Cambridge, MA 02138, USA. [11]Department of Physics, Harvard University, Cambridge, MA 02138, USA.
*These authors contributed equally to this work.
†Corresponding author. Email: yulin.chen@physics.ox.ac.uk

The crystal structure of $Co_3Sn_2S_2$ is composed of stacked …– Sn-[S-(Co_3-Sn)-S] –… layers (see Fig. 1C, space group $R\bar{3}m$, no. 166). In each [S-(Co_3-Sn)-S] layer group, the central Co layer forms a two-dimensional (2D) Kagomé lattice with an Sn atom at the center of the hexagon; S atoms are located alternately above and below the triangles formed by the Co atoms, with the adjacent [S-(Co_3-Sn)-S] layer groups linked by layer-sharing Sn atoms (Fig. 1C).

The TRS-breaking WSM phase in $Co_3Sn_2S_2$ (Fig. 1D) is caused by the joint effects of crystal field, ferromagnetism (FM), and spin-orbital coupling (SOC): The crystal field first mixes the valence band (VB) and conduction band (CB) to form fourfold degenerate nodal lines [Fig. 1D (ii), black curve]; subsequently, the degeneracy of the nodal line is lifted [Fig. 1D (iii), green curve] by the FM transition that breaks the TRS; finally, SOC splits the doubly degenerate nodal line in Fig. 1D (iii) into a pair of Weyl points with opposite chirality [Fig. 1D (iv)]. According to recent ab initio calculations for this material (*33*, *39*), there are three pairs of Weyl points within each bulk BZ connected by the SFAs (Fig. 1E).

To study the electronic structure of $Co_3Sn_2S_2$ and its magnetic WSM nature, we synthesized high-quality crystals with flat, shiny, cleaved surfaces (*40*). The temperature-dependent transport (Fig. 1F) and magnetization measurements (Fig. 1F, inset) clearly illustrate that an FM transition occurs at a critical temperature T_C = 175 K with a hysteresis loop [for additional characterization, see (*40*)].

The overall band structure of $Co_3Sn_2S_2$ obtained through ARPES is summarized in Fig. 2. The experimental stacking plots of constant energy contours of the electronic bands at different binding energies (Fig. 2A) show sophisticated structures and their evolution with energy. To understand these rich details, we performed ab initio calculations [for details, see (*40*)] for the bulk electronic bands for comparison. As shown in Fig. 2, B to D, the experimental results and calculations show good overall agreement, except for the triangle-shaped Fermi surface (FS) pieces around the $\bar{K}$ and $\bar{K}'$ points, which were observed in experiments (Fig. 2C) but absent in the bulk calculations. These unusual FS pieces, as we will demonstrate below, arise from the topological surface states that will result in characteristic SFAs.

After establishing the overall correspondence between the experimental and calculated (bulk) band structures, we now focus on the vicinity of the triangle-shaped FSs by performing fine ARPES

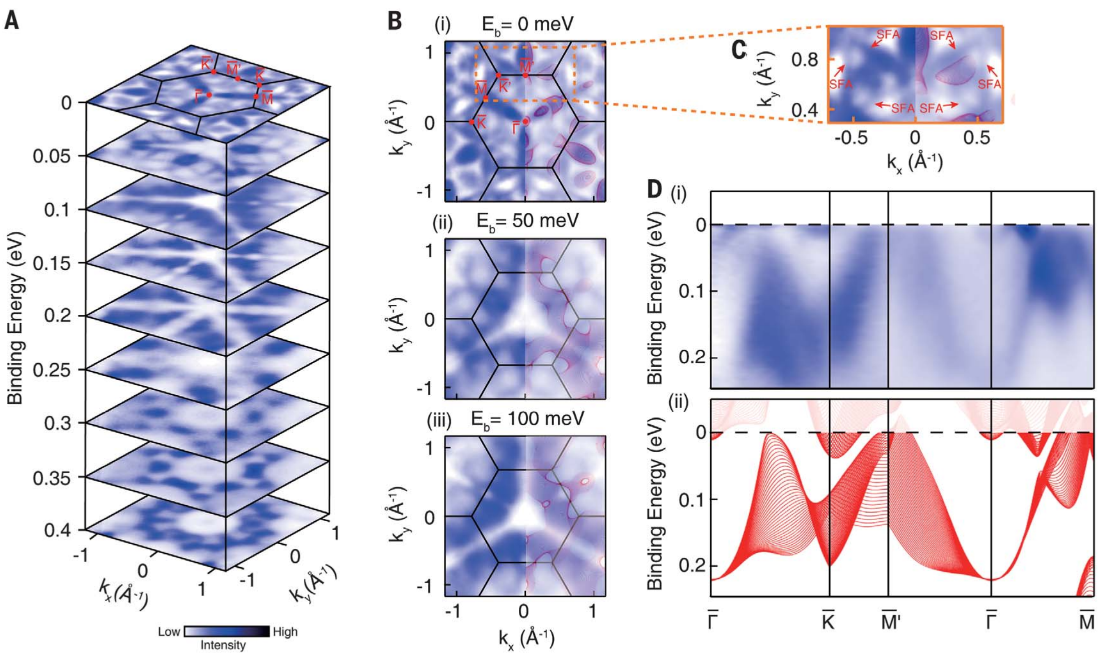

Fig. 2. General electronic structure and band evolution with binding energy. (**A**) Stacking plots of constant energy contours at different binding energies obtained from ARPES show sophisticated band structure evolution. (**B**) Comparison between three experimental constant energy contours at different binding energies [(i) to (iii)] and the ab initio calculations of the bulk bands (superimposed in red on the right half of the plots), showing excellent agreement except for the triangle-shaped FSs around the $\bar{K}$ and $\bar{K}'$ points. Note that the experimental plot has been symmetrized according to the crystal symmetry for comparison with the calculation (as in Figs. 3 and 4). (**C**) Magnified Fermi surface around the $\bar{K}$ and $\bar{K}'$ points as indicated by the orange dashed line in (B) (i). The triangle-shaped FSs around the $\bar{K}$ and $\bar{K}'$ points, which are formed by SFAs, are marked by red arrows (see text for details). (**D**) Comparison of the experimental (i) and calculated (ii) band dispersions along different high-symmetry directions across the whole BZ ($\bar{\Gamma}-\bar{K}-\bar{M}'-\bar{\Gamma}-\bar{M}$), showing good agreement. The calculated bandwidth was renormalized by a factor of 1.43, and the energy position was shifted to match the experiment. The data were recorded at 10 K.

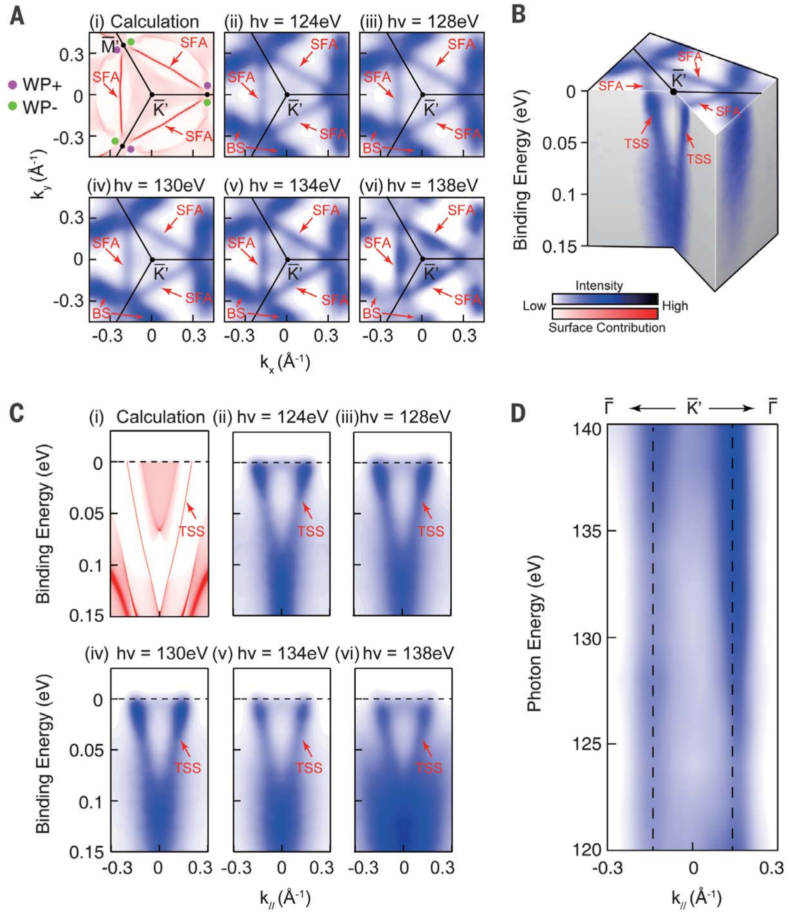

Fig. 3. Observation of the SFA and TSS dispersion on the (001) surface. (**A**) Comparison of (i) the calculated FS from both bulk and surface states and [(ii) to (iv)] the experimental FSs under different photon energies. The magenta and green dots in (i) represent the Weyl points with opposite chirality, and the SFAs are indicated by red arrows. (ii) to (vi) Experimental FSs under different photon energies all show SFAs agreeing with the calculation in (i). The triangle-shaped FSs formed by the SFAs do not change in size and shape under different photon energies, confirming their surface origin. (**B**) 3D intensity plot of the experimental band structure near the $\bar{K}'$ point. The SFAs and the dispersions of the TSSs are marked by red arrows. (**C**) Comparison of the dispersions from (i) calculated TSS along the $\bar{\Gamma} - \bar{K}' - \bar{\Gamma}$ direction and [(ii) to (vi)] the experimental TSSs. (**D**) Photon energy–dependent ARPES spectral intensity map at E_F along the $\bar{\Gamma} - \bar{K}' - \bar{\Gamma}$ direction, where the black dashed lines indicate the topological surface states that show no dispersion along the energy (and thus k_z) direction. The data were recorded at 10 K.

mapping with high resolution to study their detailed geometry and to search for the unusual SFAs, the characteristic signature of the WSM.

According to our calculations [for details, see the materials and methods section in (*40*)], the SFAs in $Co_3Sn_2S_2$ are located around the $\bar{K}'$ of the BZ [Fig. 3A, (i)], formed by a line segment that connects one pair of Weyl points with opposite chirality in each BZ. These line segments from three adjacent BZs can form a triangle-shaped surface FS piece. This unusual surface FS topology was indeed observed experimentally [Fig. 3A (ii) to (vi)], where the unchanged shape of these line-segment FS pieces from different photon energies indicates their surface origin [Fig. 3A (ii) to (vi); results from more photon energies can be found in (*40*)]. Notably, each line-segment FS piece merges into the bulk FS pockets near the $\bar{M}'$ point of the BZ [where the Weyl points are located; Fig. 3A (i)], in excellent agreement with the calculations.

In addition to the FS topology, we can study the dispersions of the topological surface states (TSSs) that result in the SFAs discussed above (Fig. 3B). The dispersions of the TSSs from different photon energies are in good agreement with calculations (Fig. 3C). Indeed, the photon energy dependent ARPES measurements (Fig. 3D) show the characteristic vertical dispersionless FS with respect to the photon energy (and thus also k_z), unambiguously confirming the surface nature of TSSs (Fig. 3C) and the triangle-shaped FS pieces [Fig. 3B; further discussion on the SFA states can be found in (*40*)].

With the SFAs identified, we next searched for the characteristic bulk Weyl fermion dispersion. For this purpose, we performed broad-range (50 to 150 eV) photon energy–dependent ARPES measurements (see (*40*) for details) to precisely identify the k_z momentum locations of the Weyl points [Fig. 4A (i)]. In Fig. 4A (ii), bulk bands with strong k_z dispersion can be seen in the k_y–k_z spectra intensity map (in contrast to the TSSs without k_z dispersion in Fig. 3D), agreeing well with our calculations [overlaid in red in Fig. 4A (ii)]. The measured dispersions along two different high-symmetry directions show good overall agreement with calculations [Fig. 4B; further discussion on the comparison can be found in (*40*)].

The agreement between experiments and calculations in Fig. 4, A and B, allows us to identify the bulk Weyl points in $Co_3Sn_2S_2$, which lie at $k_z = \pm 0.086$ Å^{-1} planes [Fig. 4A (i)] and can be accessed by using 115-eV photons (corresponding to $k_z = -0.086$ Å^{-1} in Fig. 4A). To precisely locate the in-plane momentum loci of the Weyl points, we first performed k_x-k_y FS mapping [Fig. 4C (i)] of the band structures across the surface BZ, and then we focused on band dispersions that cut through the Weyl point [see the cutting plane in Fig. 4C (i)].

Indeed, the measured bulk band dispersion is linear, matching the calculations [Fig. 4C (ii), red curve]. However, because the Weyl points are located at an energy ~50 meV above the Fermi level (E_F) for the undoped sample [Fig. 4C (ii)], to observe the band crossing at the Weyl point, we introduced in situ electron doping using an alkaline metal dozer [Fig. 4D, see (*40*) for details] and successfully raised E_F to the Weyl points. As illustrated in Fig. 4E, with the lifting of E_F, spot-like FSs (i.e., the Weyl points) emerge [Fig. 4E (i); at this photon energy, the FS mapping only cuts across three bulk Weyl points at $k_z = -0.086$ Å^{-1} plane, as shown in Fig. 4A (i)]. The band dispersion in Fig. 4E (ii) also shows the linear crossing of the bands at the Weyl point, in good agreement with the calculations.

The observation of the distinctive SFAs and bulk Weyl points with linear dispersions, together with the overall agreement of the measurements with theoretical calculations, establishes $Co_3Sn_2S_2$ as a magnetic WSM. This finding extends the possibilities for the exploration of other exotic phenomena associated with TRS-breaking WSMs (such as the unusually large AHC and QAH effects at the 2D limit) and potential applications. In addition, the topological phase transition across the FM ordering and the detailed spin textures of the SFAs in $Co_3Sn_2S_2$ merit further investigation.

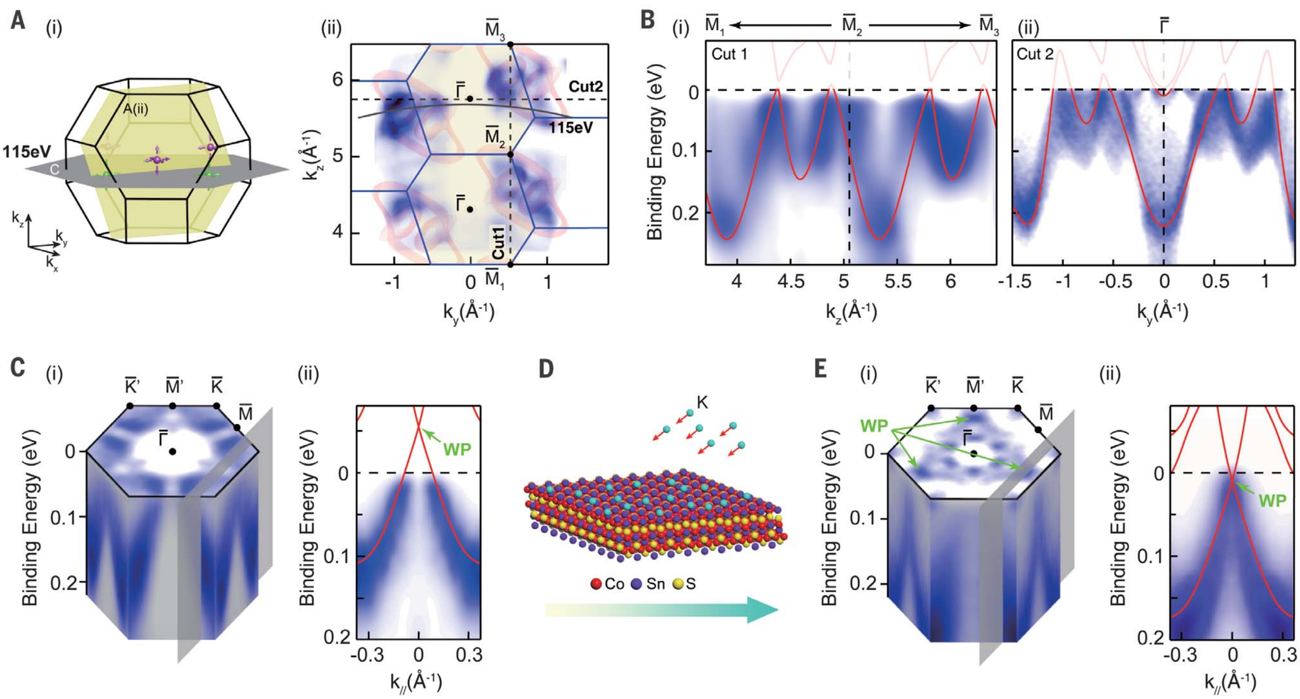

Fig. 4. Bulk-band structure and observation of the Weyl point. (**A**) (i) Schematic of the measurement k_y-k_z plane (vertical yellow plane) of the intensity plot in (ii). Weyl points are also illustrated, with the reference k_x-k_y plane (horizontal gray plane, corresponding to 115-eV photons) used to help show their locations. (ii) Photoemission intensity plot along the k_y-k_z plane [yellow plane in (i)]. Energy integration window from E_F – 100 meV to E_F is shown. Overlaid red contours are calculated bulk FSs with the same energy integration window, showing overall agreement with the experiment. The black curves indicate the k_z momentum locations probed by 115-eV photons. The two dashed lines marked as "cut1" and "cut2" indicate the momentum direction of the two band dispersions shown in (B). (**B**) Bulk-band dispersions along two high-symmetry directions, indicated as cut1 and cut2 in (A), (ii), respectively. The calculated band dispersions (red curves) are overlaid. (**C**) (i) 3D ARPES spectra intensity plot measured with 115-eV photon energy, showing both the FS (top surface) and the band dispersions (side surfaces). The gray plane indicates the location of the band dispersion cut in (ii). (ii) Band dispersion showing linear dispersions toward the Weyl point above the E_F, in agreement with the calculations (red curves overlaid). (**D**) Illustration of the in situ electron doping using an alkaline (potassium) metal dispenser. (**E**) (i) 3D ARPES spectra intensity plot measured after potassium dosing, which lifted E_F; Weyl points now emerge (marked by green arrows). (ii) The measured band now shows a linear dispersion across the Weyl point, agreeing well with the calculations (red curves overlaid). The calculated bandwidth was renormalized by a factor of 1.43 and the energy position was shifted to match the experiment. The data were recorded at 10 K.

REFERENCES AND NOTES

1. G. E. Volovik, *The Universe in a Helium Droplet* (Oxford Univ. Press, 2003).
2. K. S. Novoselov, *Angew Chem. Int. Ed. Engl.* **50**, 6986–7002 (2011).
3. M. Z. Hasan, C. L. Kane, *Rev. Mod. Phys.* **82**, 3045–3067 (2010).
4. X.-L. Qi, S.-C. Zhang, *Rev. Mod. Phys.* **83**, 1057–1110 (2011).
5. N. P. Armitage *et al.*, *Rev. Mod. Phys.* **90**, 015001 (2018).
6. X. Wan *et al.*, *Phys. Rev. B Condens. Matter Mater. Phys.* **83**, 205101 (2011).
7. H. Weng *et al.*, *Phys. Rev. X* **5**, 011029 (2015).
8. S.-M. Huang *et al.*, *Nat. Commun.* **6**, 7373 (2015).
9. S.-Y. Xu *et al.*, *Science* **349**, 613–617 (2015).
10. B. Q. Lv *et al.*, *Phys. Rev. X* **5**, 031013 (2015).
11. L. X. Yang *et al.*, *Nat. Phys.* **11**, 728–732 (2015).
12. A. A. Zyuzin, A. A. Burkov, *Phys. Rev. B Condens. Matter Mater. Phys.* **86**, 115133 (2012).
13. C.-X. Liu, P. Ye, X.-L. Qi, *Phys. Rev. B Condens. Matter Mater. Phys.* **87**, 235306 (2013).
14. K. Landsteiner, *Phys. Rev. B Condens. Matter Mater. Phys.* **89**, 075124 (2014).
15. A. C. Potter *et al.*, *Nat. Commun.* **5**, 5161 (2014).
16. P. Hosur, *Phys. Rev. B Condens. Matter Mater. Phys.* **86**, 195102 (2012).
17. A. Cortijo *et al.*, *Phys. Rev. Lett.* **115**, 177202 (2015).
18. A. G. Grushin *et al.*, *Phys. Rev. X* **6**, 041046 (2016).
19. D. I. Pikulin *et al.*, *Phys. Rev. X* **6**, 041021 (2016).
20. H. Shapourian, T. L. Hughes, S. Ryu, *Phys. Rev. B Condens. Matter Mater. Phys.* **92**, 165131 (2015).
21. G. Xu *et al.*, *Phys. Rev. Lett.* **107**, 186806 (2011).
22. Z. Wang *et al.*, *Phys. Rev. Lett.* **117**, 236401 (2016).
23. A. A. Soluyanov *et al.*, *Nature* **527**, 495–498 (2015).
24. G. Chang *et al.*, *Phys. Rev. B* **97**, 041104 (2018).
25. Z. K. Liu *et al.*, *Nat. Mater.* **15**, 27–31 (2016).
26. J. Jiang *et al.*, *Nat. Commun.* **8**, 13973 (2017).
27. L. Huang *et al.*, *Nat. Mater.* **15**, 1155–1160 (2016).
28. A. Tamai *et al.*, *Phys. Rev. X* **6**, 031021 (2016).
29. Y. Machida *et al.*, *Nature* **463**, 210–213 (2010).
30. E. Y. Ma *et al.*, *Science* **350**, 538–541 (2015).
31. T. Kondo *et al.*, *Nat. Commun.* **6**, 10042 (2015).
32. P. Hosur, X.-L. Qi, *C. R. Phys.* **14**, 857–870 (2013).
33. E. Liu *et al.*, *Nat. Phys.* **14**, 1125–1131 (2018).
34. Q. Wang *et al.*, *Nat. Commun.* **9**, 3681 (2018).
35. J. Kübler, C. Felser, *EPL* **114**, 47005 (2016).
36. A. A. Burkov, L. Balents, *Phys. Rev. Lett.* **107**, 127205 (2011).
37. K. Kuroda *et al.*, *Nat. Mater.* **16**, 1090–1095 (2017).
38. M. Yao *et al.*, Switchable Weyl nodes in topological Kagome ferromagnet Fe_3Sn_2. arXiv:1810.01514 [cond-mat-str-el] (2 October 2018).
39. Q. Xu *et al.*, *Phys. Rev. B* **97**, 235416 (2018).
40. See supplementary materials.
41. D. Liu, Replication Data for: Magnetic Weyl Semimetal Phase in a Kagomé Crystal, Version 1, Harvard Dataverse (2019).

ACKNOWLEDGMENTS

We thank B. H. Yan for insightful discussions and acknowledge Diamond Light Source beamline I05 (proposal nos. SI22367 and SI20683), Advanced Light Source (U.S. DOE Office of Science User Facility under contract no. DE-AC02-05CH11231) BL10.0.1., Stanford Synchrotron Radiation Laboratory (DOE Office of Science User Facility under contract no. DE-AC02-76SF00515) BL5-2, and Shanghai Synchrotron Radiation Facility beamline 03U (National Natural Science Foundation of China under contract no. 11227902) for access. **Funding:** This work was supported by the Shanghai Municipal Science and Technology Major Project (grant no. 2018SHZDZX02 to Y.L.C., A.J.L., and Z.K.L.), the Alexander von Humboldt Foundation (to D.F.L.), the National Natural Science Foundation of China (grant nos. 11774190, 11634009, 11674229, and 11974394 to L.X.Y., Y.L.C., Z.K.L., and E.K.L.), the National Key R&D Program of China (grant nos. 2017YFA0305400 and 2017YFA0206303 to Z.K.L. and E.K.L.), the Tsinghua University Initiative Scientific Research Program (to Y.L.C. and L.X.Y.), and the Wurzburg-Dresden Cluster of Excellence on Complexity and Topology in Quantum Matter (EXC 2147, no. 39085490 to C.F.). **Author contributions:** Y.L.C. conceived the project. D.F.L. and A.J.L. performed the ARPES experiments with the assistance of Y.W.L., C.C., D.P., and E.K.L. Q.N.X., W.J.S., and Y.S. performed ab initio calculations. E.K.L. synthesized and characterized the single crystals. S.K.M., P.D., T.K., and C.C. provided the beamline support. L.X.Y., Z.K.L., G.L., S.S.P.P., and C.F. contributed to the scientific discussions. **Competing interests:** The authors declare no competing interests. **Data and materials availability:** All data presented in this paper are available from Harvard Dataverse (*41*).

SUPPLEMENTARY MATERIALS

science.sciencemag.org/content/365/6459/1282/suppl/DC1
Materials and Methods
Supplementary Text
Figs. S1 to S7
Table S1
References (*42–50*)

2 September 2018; accepted 14 August 2019
10.1126/science.aav2873

Science

Magnetic Weyl semimetal phase in a Kagomé crystal

D. F. Liu, A. J. Liang, E. K. Liu, Q. N. Xu, Y. W. Li, C. Chen, D. Pei, W. J. Shi, S. K. Mo, P. Dudin, T. Kim, C. Cacho, G. Li, Y. Sun, L. X. Yang, Z. K. Liu, S. S. P. Parkin, C. Felser and Y. L. Chen

Science **365** (6459), 1282-1285.
DOI: 10.1126/science.aav2873

Magnetic Weyl semimetals

Weyl semimetals (WSMs)—materials that host exotic quasiparticles called Weyl fermions—must break either spatial inversion or time-reversal symmetry. A number of WSMs that break inversion symmetry have been identified, but showing unambiguously that a material is a time-reversal-breaking WSM is tricky. Three groups now provide spectroscopic evidence for this latter state in magnetic materials (see the Perspective by da Silva Neto). Belopolski *et al.* probed the material Co_2MnGa using angle-resolved photoemission spectroscopy, revealing exotic drumhead surface states. Using the same technique, Liu *et al.* studied the material $Co_3Sn_2S_2$, which was complemented by the scanning tunneling spectroscopy measurements of Morali *et al.* These magnetic WSM states provide an ideal setting for exotic transport effects.

Science, this issue p. 1278, p. 1282, p. 1286; see also p. 1248

Science (print ISSN 0036-8075; online ISSN 1095-9203) is published by the American Association for the Advancement of Science, 1200 New York Avenue NW, Washington, DC 20005. The title *Science* is a registered trademark of AAAS.